FULL PAPER

Carbon-Nanotube-Templated Microfabrication of Porous Silicon-Carbon Materials with Application to Chemical Separations

*Jun Song, David S. Jensen, David N. Hutchison, Brendan Turner, Taylor Wood, Andrew Dadson, Michael A. Vail, Matthew R. Linford, Richard R. Vanfleet, and Robert C. Davis**

Carbon-nanotube-templated microfabrication (CNT-M) of porous materials is demonstrated. Partial chemical infiltration of 3D carbon-nanotube structures with silicon results in a mechanically robust material, structured from the 10 nm scale to the 100 μm scale. The nanoscale dimensions are determined by the diameter and spacing of the resulting silicon/carbon nanotubes, while the microscale dimensions are controlled by the lithographic patterning of the CNT growth catalyst. We demonstrate the utility of this hierarchical structuring approach by using CNT-M to fabricate thin-layer-chromatography (TLC) separations media with precise microscale channels for fluid-flow control and nanoscale porosity for high analyte capacity. Chemical separations done on the CNT-M-structured media outperform commercial high-performance TLC media.

1. Introduction

Several functional properties of materials are impacted by the 3D shape of the material on both the micrometer scale (microscale) and the nanometer scale (nanoscale). The microscale patterning of a material affects several functional properties including fluid flow, ion and electron conductivity, the mechanical response, and interactions with electromagnetic fields and waves.[1,2] Nanoscale structuring can dramatically change chemical-reaction rates and the surface-adsorption capacity, as the surface-to-volume ratio significantly increases.[3] Electronic material properties, including the band structure, recombination rates, and mobilities are strongly influenced by nanoscale structuring.[4] Often, multiple physical properties are coupled and are jointly influenced by nanoscale structuring, as is the case for strained silicon: nanoscale strain control is used to produce higher mobilities than achievable in the bulk.[5] Coupling between strain and electrochemical properties was observed in nanoscale silicon particles deposited on carbon nanotubes, which resulted in improved electrochemical cycling over bulk silicon anodes for lithium-ion batteries.[6]

Since both micro- and nanoscale structuring influences functional material properties, the ability to control microscale shape in a variety of nanostructured materials will enable a wide range of applications. Precise 3D microscale structures have been widely fabricated by reactive ion etching (RIE), wherein bulk semiconductor, metal, and ceramic materials are micromachined into the desired shapes.[7] Deep reactive ion etching has resulted in high-aspect-ratio structures in silicon.[8] Vertically aligned carbon nanotubes grown from micropatterned catalyst layers result in high-aspect-ratio structures with vertical sidewalls.[9,10] However, the as-grown nanotube density is low and the tubes are held to each other only by weak van der Waals forces, resulting in structures that are too weak to maintain their microscale shape when put in contact with fluids. Recently, templated microfabrication of robust, high-aspect-ratio structures in silicon, silicon nitride, and carbon has been done using carbon-nanotube (CNT) frameworks.[11] On the nanoscale, silicon materials including silicon nanowires (SiNWs),[12] silicon nanotubes (SiNTs),[13] and porous silicon[14] have previously been fabricated by a variety of methods including chemical vapor deposition,[12,15] template-assisted growth,[16] solution-phase synthesis,[17] and electrochemical etching.[14] Vertically etched porous silicon has been used to produce microscale features with vertical nanopores by masking and plasma etching.[18] Carbon nanotubes also have been used as a nanoscale template for various materials, including polymers,[19] metals,[20] metal alloys,[21,22] and silicon.[23–26] While these prior methods have been used to fabricate structures on the nano- and microscales, there has not been a general, flexible method for 3D patterning that spans the entire range of sizes.

J. Song, D. N. Hutchison, B. Turner, T. Wood, M. R. Linford
Dr. R. R. Vanfleet, Dr. R. C. Davis
Department of Physics and Astronomy
Brigham Young University
Provo, UT 84602
E-mail: davis@byu.edu
D. S. Jensen
Department of Chemistry and Biochemistry
Brigham Young University
Provo, UT 84602
A. Dadson, Dr. M. A. Vail
US Synthetic Corporation
Orem, Utah 84058

DOI: 10.1002/adfm.201001851

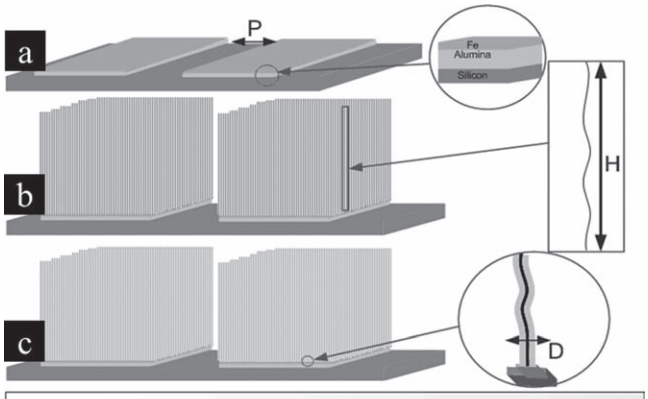

d

Patterned SiCNT Dimensions

	Minimum	Maximum
Pattern (P)	0.5 um	10 cm
Height (H)	10 um	1 mm
Diameter (D)	10 nm	120 nm

Figure 1. Patterning 3D structures with control over a hierarchical set of length scales. a–c) Diagram of the fabrication process for patterned SiCNTs using a vertical CNT template: photolithography, deposition and a lift-off process yields a 2D alumina and iron catalyst layer (a); CNTs grow vertically from the patterned catalyst and form a 3D structure (b); SiCNTs are formed by coating the CNTs with Si by low-pressure chemical vapor deposition (LPCVD) (c). d) The fabrication dimensions can be controlled over several length scales as outlined in the table, and limited only by the lithography system.

Here, we introduce a fabrication process that results in control over the length scale ranging from several nanometers to several hundred micrometers. The process, called carbon-nanotube-templated microfabrication (CNT-M) uses partial Si infiltration of the carbon-nanotube frameworks to fabricate porous, 3D, microscale shapes consisting of silicon-carbon core-shell nanotubes (SiCNTs) as illustrated in **Figure 1**a–c. The addition of thin silicon shells to the vertically aligned CNTs (VACNTs) enables the fabrication of robust silicon nanostructures with the flexibility to design a wide range of geometries by CNT-M. Figure 1 illustrates the hierarchical nature of the geometry and the ability to control the geometric dimensions over a broad range of length scales.

We illustrate the utility of this hierarchical structuring approach by fabricating micropatterned plates for a chemical-separation technique: high-resolution thin-layer chromatography (TLC). In TLC, samples are spotted near the bottom of a plate and carried up the plate by solvent fluid flow by capillary action. If the solvent (mobile phase) and materials in the TLC plate, that is to say, the stationary phase, are chosen correctly, different analytes move up the plate at different speeds resulting in separated spots when multiple analytes are present. In TLC, the separation mechanism results from different equilibrium constants of analytes partitioning themselves between the mobile and stationary phases. Spatial non-uniformity in the fluid flow spreads each TLC analyte spot, resulting in low resolution. Consequently, high-resolution separations require control of structure on the microscale for uniform solvent flow.[27] High-resolution TLC (at practical concentrations) requires a nanostructured, high-area surface to keep the surface from overloading with analyte and consequently spreading the analyte spot. Commercial TLC plates are fabricated by coating glass or metal surfaces with porous silica microparticles. The miroparticles are deposited on the surface under carefully controlled processes and held together with a binder (e.g., gypsum or poly(vinyl alcohol)). Although commercial TLC is a mature technology, there is significant room for improvement in the microstructure regularity when compared to lithographically defined structures. Structures have previously been microfabricated for chromatography, but the lack of nanoscale porosity severely limits the capacity of these structures.[28] Here, we have constructed binder-free TLC plates using an extension of the CNT-M process. The extension adds a thermal-oxidation step after Si infiltration; the oxidation step converts the Si to silica and removes the carbon nanotubes. TLC was performed on the resulting silica plates, showing improvement over commercial high-performance TLC (HPTLC) plates.

2. Results and Discussion

Low-pressure chemical-vapor-deposition (LPCVD) silicon forms remarkably uniform films around patterned multiwalled carbon nanotubes (MWCNTs); **Figure 2** shows typical SEM images of patterned silicon-carbon core-shell-nanotube structures. The SiCNTs are vertically aligned and retain the vertical orientation of the initial CNT forest. Complex 3D structures and lines of vertical SiCNTs are shown in Figure 2a and 2b. The height of the synthesized SiCNTs is controlled by varying the run time for the carbon-nanotube growth. For example, 2 min growth resulted in 100 μm high CNTs. The SiCNT diameter can be

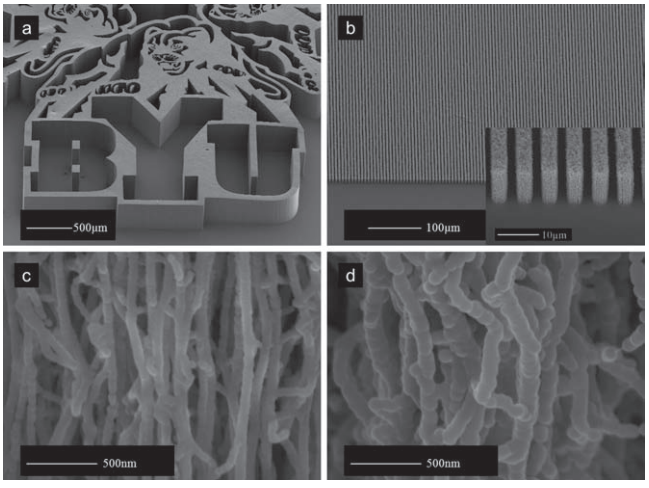

Figure 2. SEM images of patterned SiCNTs. a) An arbitrary 2D catalyst pattern results in a robust 3D SiCNT structure, in this case a 400 μm high BYU logo. b) Lines of 10 μm tall, vertical SiCNTs are shown. Close-up views of (b) are shown in the inset. c) High-magnification view shows SiCNTs synthesized with LPCVD silicon at 530 °C for 60 min, which deposits a thin Si coating and results in 70 nm diameter SiCNTs. d) SiCNTs synthesized with LPCVD silicon at 560 °C for 60 min, which deposits a thicker Si coating and results in 120 nm diameter SiCNTs.

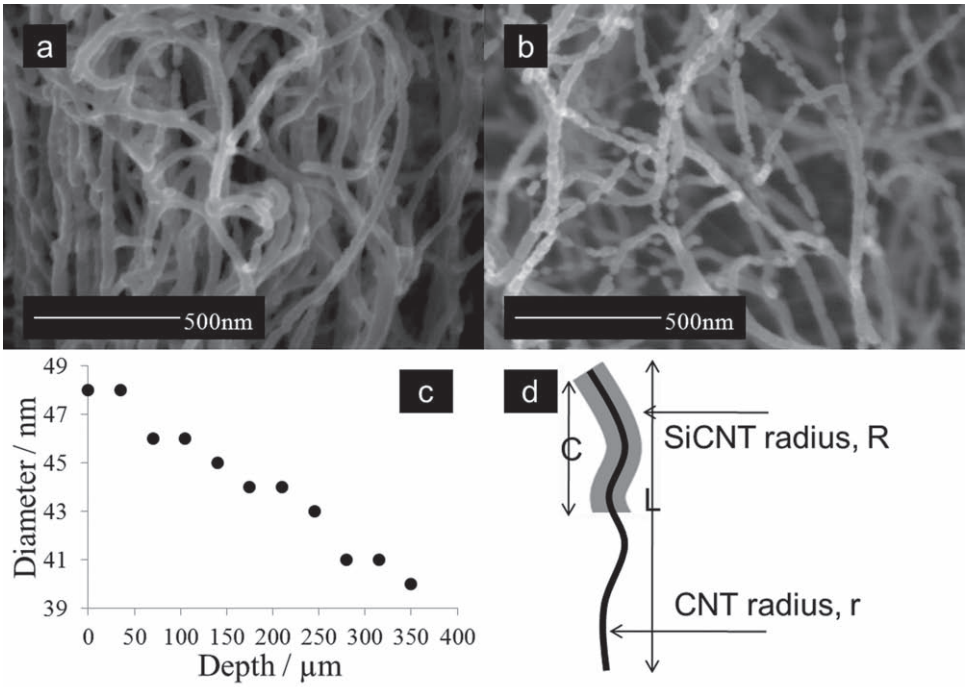

Figure 3. An unpatterned CNT forest was grown to a height of 400 µm and coated with silicon at 530 °C for 40 min. a) The SEM image of the top of the SiCNTs shows a uniform coating. b) The morphology of most tubes near the bottom is smooth, but there also are some discrete silicon beads. c) The SiCNT diameter was measured at various depths in the structure. The diameter of the SiCNTs decreases and a more-beadlike morphology is seen at greater depths. d) A sketch shows the parameters used to calculate the volume of deposited silicon.

from 10 nm to 120 nm, and depends on the LPCVD process parameters and time. Figure 2c and 2d are close-up views of SiCNTs with thinner (2c) and thicker (2d) silicon films deposited at 530 °C and 560 °C for 60 min. The 560 °C LPCVD process has a higher deposition rate and therefore grows a thicker silicon coating. The structure of the SiCNTs is generally vertical with individual nanotubes in the structure following an undulating path, as seen in Figure 2c and 2d.

LPCVD is known to produce conformal coatings with excellent penetration into cracks and porous structures. Our results also show excellent penetration into the CNT forest, though the thickness and morphology of the silicon coating under the conditions used does depend somewhat on depth (and distance from the pattern edges) into the carbon nanotube forest, as shown in **Figure 3**. The Si coating of the CNTs is compared between the top (a) and bottom (b) regions of the forest. In Figure 3a, the top region shows a uniformly thick coating; in Figure 3b, the thinner coating is generally smooth, but, in places, is discrete like beads on a string. Figure 3c plots the SiCNT diameter at various depths in the structure showing that, deep in the structure, the deposition rate is lower. We define the diameter of the SiCNTs as the average width of the tubes (top of the forest) or beads (bottom of the forest). The average diameter of the SiCNTs ranges from 48 nm on the top to 40 nm at the bottom for this deposition. The diameter and morphology variance arises from differences in the silicon deposition rate from the top to the bottom. To determine the difference in silicon-deposition rate, we calculate the silicon volume per nanotube length using Equation 1.

$$\frac{V}{L} = \pi(R^2 - r^2)\frac{C}{L} \quad (1)$$

In the above formula, V/L is the silicon volume per unit length of nanotube, R is the radius of the SiCNTs, r is the radius of the CNTs, and C is the fraction of the nanotube length coated with silicon. All of the parameters here are illustrated in Figure 3d. From an analysis of the 40 min Si deposition at 530 °C shown in Figure 3a and 3b, V/L on the top is about 1750 nm^2, and at the bottom of the 400 µm forest, V/L is about 900 nm^2, approximately half of that on the top. Methods of increasing the deposition uniformity are discussed below.

The structural characteristics of the SiCNTs were investigated using Raman spectroscopy. Raman spectra of vertically aligned SiCNTs are shown in **Figure 4** for both amorphous and crystalline samples. The amorphous silicon peak is centered at 465 cm^{-1} and seen in Figure 4a and 4b. Because of the amorphous structure, the momentum-selection rule is relaxed, and a broad peak is seen. In crystalline silicon, only the 64 meV optical phonon is allowed,[29] resulting in a sharp peak at 517 cm^{-1} and a broad feature at 945 cm^{-1}, seen in Figure 4c. The peak at 517 cm^{-1} due to crystalline SiCNTs is slightly broader and more asymmetric than that of bulk silicon, which is consistent with Raman measurements of silicon nanowires.[30,31] All three Raman spectra show the first-order D band (1305 cm^{-1}) and G band (1587 cm^{-1}) of the carbon nanotubes. Increasing the thickness of the silicon gives a corresponding increase in the silicon signal and decreases the CNT signal. Additionally, the relative intensities of the D and G bands change as the

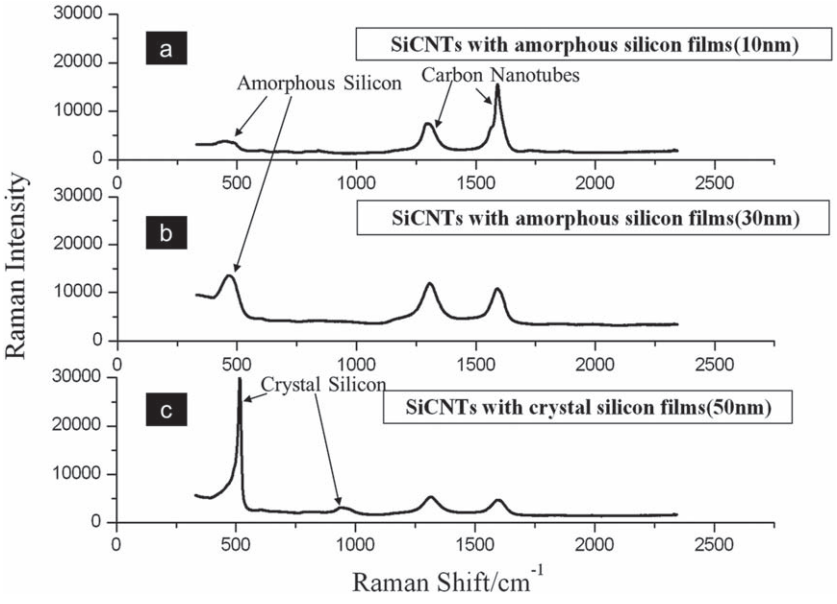

Figure 4. a,b) 10 nm and 30 nm of amorphous silicon deposited at 530 °C. The Raman spectrum peak due to amorphous silicon (α-si) is shown. With a thicker silicon shell, the peak due to silicon (around 465 cm^{-1}) is higher. c) 50 nm of crystalline silicon deposited at 560 °C and annealed at 700 °C overnight. The Raman shifts of 517 cm^{-1} and 945 cm^{-1} indicate a crystalline silicon coating. The carbon nanotubes are identifiable in each spectrum (a,b,c).

silicon thickness is increased. One question is whether a SiC layer was formed at the Si-CNT interface. SiC has many polytypes, which have different Raman spectra. The maximum-intensity folded-transverse-optical (FTO) modes for all 6 polytypes[32] fall in the range between 764 and 796 cm^{-1}, but there are no features in our spectra in this range, indicating that, within the detection limits of this instrument, there was no SiC present. Panitz et al.[33] used Raman spectroscopy in the wavenumber range from 250 to 1000 cm^{-1} to distinguish silicon carbide from silicon; our spectra are an excellent match to their silicon spectra including the broad feature just below 1000 cm^{-1}.

A series of transmission-electron-microscopy (TEM) images of SiCNTs are shown in **Figure 5**. The TEM images show two silicon morphologies after silicon deposition, either as beads formed along the CNT or a conformal shell of silicon over the CNT. Figure 5a and its inset show typical images where the multiwalled-carbon-nanotube core and the 10 nm (average) silicon coating can be seen. The fairly uniform silicon coating on these carbon nanotubes gives 30 nm-wide SiCNTs with occasional bead formation. The high-resolution micrographs (b is an amorphous-silicon coating and c is a crystalline-silicon coating) show the morphology of these SiCNTs, and the inset in Figure 5c shows the selected-area-electron-diffraction (SAED) pattern of that specimen, showing its polycrystalline nature.

Scanning transmission-electron-microscopy (STEM) images and electron-energy-loss-spectroscopy (EELS) data are shown in **Figure 6**. In Figure 6a, the annular dark-field image shows a horizontally oriented SiCNT. The core-shell structure seen in projection should have a dip in intensity at the carbon core, as seen. The line in Figure 6a is the location of the EELS line scan shown in Figure 6b and 6c. In Figure 6c, an EELS spectrum is shown from the middle of the SiCNT. In the data shown, the decreasing background has been fitted to the region before the silicon edge and subtracted from the entire spectrum. The silicon peak is just above (higher energy loss) the background window. The fine structure of the silicon peak is consistent with crystalline silicon. The carbon peak is also labelled on the right half of the spectrum and its fine structure is consistent with that of carbon nanotubes.[34] In the middle of the spectrum is an artifact that arises from a mismatch between the quadrants of the EELS charge-coupled-device (CCD) readout. We include the full spectrum (with artifact) to show that the silicon and carbon data come from the same data set with perfect spatial registry. With the background subtraction as shown in Figure 6c, the counts in the silicon peak (over some region close to the edge onset) are proportional to the number of silicon atoms seen by the beam. Figure 6b shows the number of counts in the silicon edge along the line scan. Also in Figure 6b, the carbon-edge counts are shown. The carbon data used the same data sets but with the background subtraction taken just before the carbon edge, and the counts were then collected from near the carbon-edge onset. The two lines in Figure 6b show the distribution of silicon and carbon across the SiCNT. The silicon shows a dip in the middle of its distribution with a corresponding increase in carbon at the edges of the dip. The carbon also shows a dip in the middle of its distribution. This profile is what would be expected from the "tube" nature of both the silicon and CNT structure.

The data shown for the Raman spectroscopy, EELS and imaging results are consistent with the proposed pictures

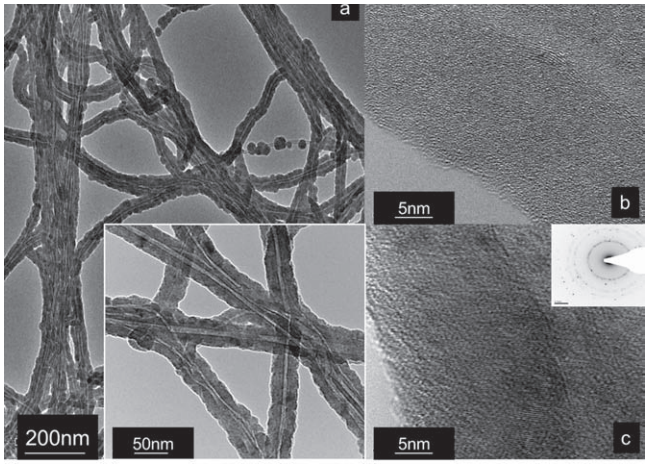

Figure 5. a) A TEM image of SiCNTs with a 10 nm silicon coating are shown. The inset shows an enlarged view of the SiCNTs. b) The high-magnification image shows the morphology of the SiCNTs coated with amorphous silicon. c) Polycrystalline-silicon-coated carbon nanotubes are proved by the SAED (Inset in c, see Figure S2 in the Supporting Information for SAED details).

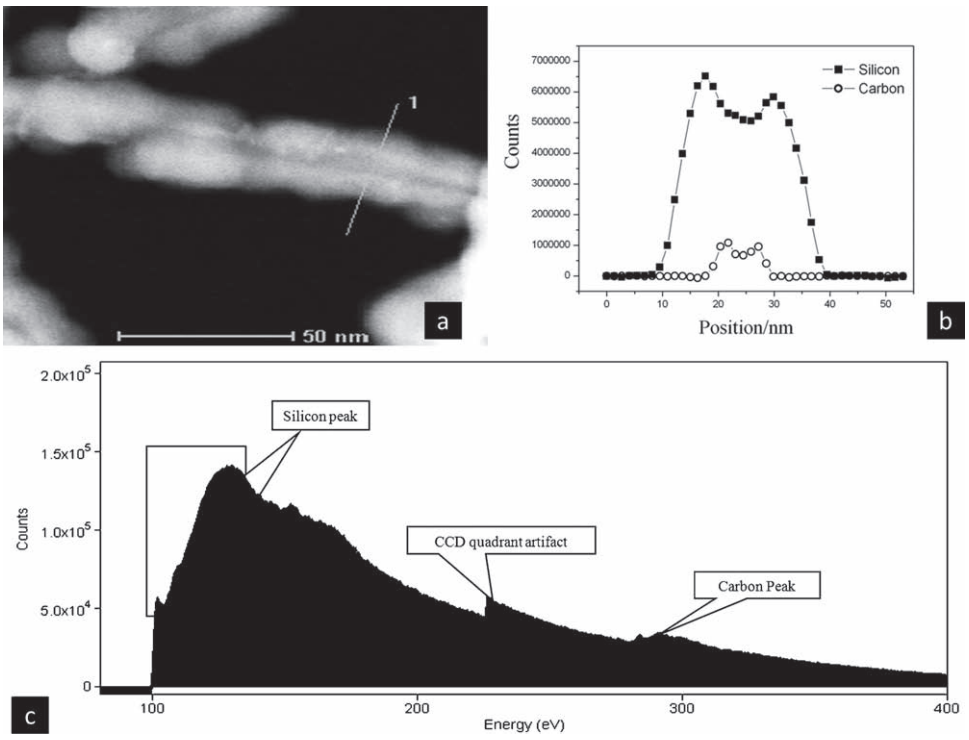

Figure 6. a) Dark-field image of an individual SiCNT by STEM. An EELS measurement was made at each point as the beam was scanned through the SiCNT along cross section line 1. b) Counts above background in the Si and the C peaks are plotted vs. position along this scan line. The percentage of silicon and carbon varies along this cross-section of the SiCNT. c) EELS near the core of the SiCNTs shows both silicon peaks and carbon peaks (from the CNTs).

of carbon nanotubes coated with amorphous or polycrystalline silicon. The coating rate is weakly dependent on depth, and the rate should also depend on the CNT pattern as well as the parameters of the LPCVD process. We have seen some evidence that lower LPCVD temperatures coat more slowly but more uniformly. To achieve uniform SiCNT diameters, the deposition rate must be limited by the kinetics of surface growth, rather than the transport of gases to and from the CNT surface. Patterning gas-access holes has previously been shown to improve gas transport and silicon-infiltration uniformity.[11] We have also observed that gas-access holes improve the SiCNT diameter uniformity. The average spacing between CNTs in this process is 100–150 nm, thus limiting SiCNT diameters to 200 nm, at which point the structure is mostly filled.

Silicon deposition on the CNTs typically forms a conformal coating but occasionally results in separated beads along the CNTs, as seen in Figure 3b and Figure 5a. This bead formation may be due to insufficient coating, a smaller diameter of the underlying nanotubes or a combination of these factors. In general, droplet or bead formation on a fiber depends upon the atoms having sufficient mobility to form the energetically preferred structure, the relative surface energies, and on the diameter of the fiber.[35] In our CNT-growth process, multiwalled CNTs were formed with a distribution of tube diameters (averaging 8 to 10 nm in diameter). We suggest that, at the Si deposition temperature (>500 °C), silicon atoms have sufficient mobility to form beads of silicon on the multiwalled CNTs. Those initially formed beads then grow and combine to form conformal coatings. The specifics of this bead-to-conformal coating process will depend upon the individual CNT diameter, the deposition temperature, and the amount of silicon on the CNT. In Figure 3, we estimate that at 530 °C our typical CNT (8 to 10 nm in diameter) is conformally coated after approximately 15 nm of deposition (40 nm total diameter including the CNT).

We applied the CNT-M process to fabricate plates for thin-layer chromatography (TLC). The SiCNTs were grown in a herring-bone pattern, as shown in **Figure 7**a–b. The resulting pattern has the right microscale shape for TLC: open channels for rapid fluid flow and thin porous walls for rapid analyte diffusion and interaction. The high nanoscale porosity and corresponding high surface area are also important for high analyte capacity. Higher-magnification imaging (Figure S5 in the Supporting Information) shows that the infiltration uniformity, top to bottom, is very good. A significant problem, however, is that the SiCNT forest is optically dark, whereas TLC plates are typically white for easy visualization of the analyte spots. To reduce optical absorption, the SiCNT structure was annealed in air to convert the silicon to silica and oxidize the CNTs. As shown in Figure 7c, the 3D herring-bone pattern was preserved through the oxidation step and the samples are optically white. The high-temperature oxidization process did cause a volume

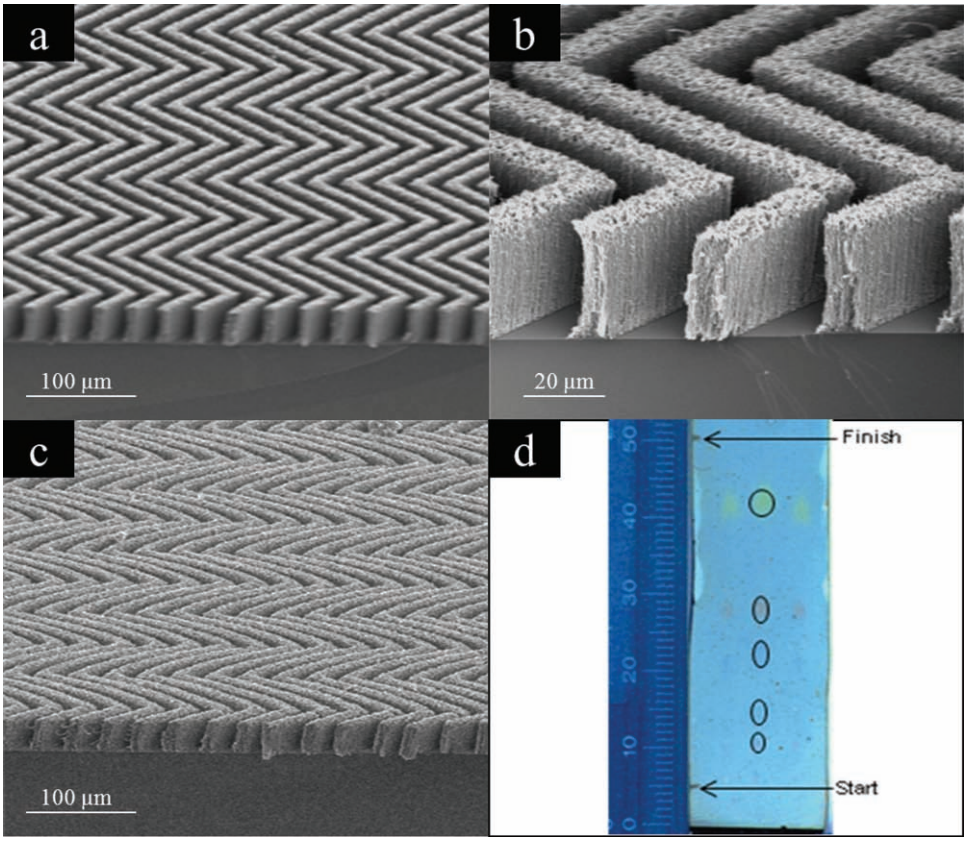

Figure 7. SiCNTs-based chromatography plates. a,b) The herring-bone CNT pattern was partially infiltrated with silicon for 80 min resulting in 4 μm hedges and 7 μm spaces. c) The herring-bone pattern after annealing at 1000 °C for 5 h in air for oxidation of the silicon and the nanotubes. The resulting structure consists entirely of SiO_2 nanowires. d) Separation of a CAMAG dye test mixture.

expansion resulting in the features becoming wider. In our TLC experiments, we used mask designs that compensated for this expansion. TEM analysis of the oxidized materials confirmed that the silicon was converted to silicon oxide and that the CNTs were removed. SEM images of the chromatographic material are shown in Figure 7d along with a demonstration of the TLC plate performance in separating a series of dyes. The CNT-M plate performance was compared with commercial TLC and HPTLC plates using two quantitative figures of merit: the TLC efficiency and the retention factor. The efficiency (number of theoretical plates, N) and retention factor (R_f) for each analyte were calculated for CNT-M TLC, commercial HPTLC, and commercial TLC plates and are illustrated in **Figure 8**. The efficiency was calculated using Equation 2, where z is the distance the analyte travels, l is the distance the solvent front travels (migration distance), and w is the chromatographic width of the analyte in the direction of the solvent front.

$$N = 16\frac{zl}{w^2} \tag{2}$$

The retention factor was calculated using Equation 3, where z is the distance the analyte travels and l is the distance the solvent front travels:

$$R_f = \frac{z}{l} \tag{3}$$

These 3D, patterned silica structures demonstrate chromatographic efficiencies that either equal or exceed those of HPTLC and exceed those of commercial TLC plates. In addition to the increased efficiencies that have been demonstrated, there was also an improvement in the speed of the separation. To analyze the features that allow CNT-M plates to outperform commercial plates, we refer to the van Deemter equation (Equation 4) for plate height (H):

$$H = A + \frac{B}{v} + C \cdot v \tag{4}$$

A smaller plate height will result in a larger number of plates and a corresponding higher efficiency. The first term in the equation, the A term, is the eddy diffusion term and is caused by differences in fluid path length taken by different solute molecules. In microstructured media, these path-length differences result from inhomogeneities in the microscale structure, which, for us, are minimized due to the precisely controlled microscale patterns of the CNT-M plates. The contribution from the second term, the B term, relates to longitudinal diffusion and is reduced at higher flow velocities. The CNT-M plates had much-shorter development times corresponding to higher velocities and therefore a reduction in the diffusion-term contribution is expected. These higher velocities were possible because the CNT-M structures could be fabricated with wider, more-direct flow channels than particulate media. The

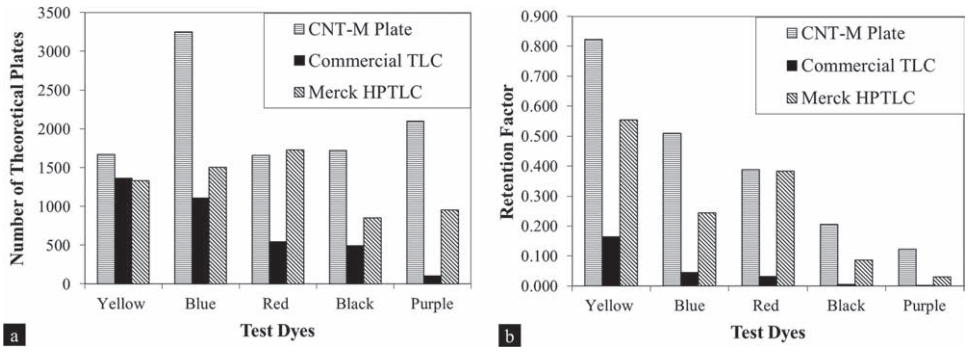

Figure 8. The efficiency (number of theoretical plates, *N*) and retention factor (R_f) for each analyte are compared between CNT-M TLC, TLC, and HPTLC plates. (The color names on the *x*-axis from yellow to purple represent different analytes in dyes.)

last term, the *C* term, comes from the mass-transfer kinetics of the analyte between the mobile and stationary phases and is reduced by decreasing the particle size, or, in our case, the hedge width. Our hedge width is nominally 4 um wide for the CNT-M plates analyzed. This is smaller than the particle sizes of both of the commercial plates. The commercial TLC plates had particles with diameters ranging from 5 to 20 μm and the HPTLC plates had particles ranging from 6 to 8 μm. Therefore the *C* term should also be significantly lower than the *C* term for commercial TLC plates and slightly lower than the *C* term for HPTLC plates. Since this term is multiplied by the velocity *v*, there may not be an improvement in this term as CNT-M velocities are higher. Additionally the ability to controllably adjust the microscale geometry with CNT-M should provide an ideal test bed for future quantitative studies of the contribution of each of these terms to the efficiency.

3. Conclusions

In conclusion, vertically aligned and patterned silicon-carbon core-shell nanotubes have been synthesized by the CNT-M process. These SiCNTs are uniform in morphology, consisting of a multiwalled nanotube core and an amorphous or crystalline silicon shell. No evidence of a SiC layer at the interface was seen by Raman spectroscopy or EELS. Using the CNT-M process, we were able to fabricate porous SiCNT and silica structures with control over the 3D microscale shape and nanoscale porosity. We view these 3D porous structures as powerful testbeds for studying a variety of the properties of micro- and nanostructured materials, as well as chemical and physical processes on the micro- and nanoscales. Furthermore, these hierarchical structures appear promising in applications including chemical separations, catalysis, energy storage, and energy conversion. We applied the CNT-M process to fabricate silica plates for TLC that outperformed commercial HPTLC plates. It should be possible to extend the CNT-M process to microfluidics, high-performance liquid chromatography (HPLC) and ultra-high-performance liquid chromatography (UPLC).

4. Experimental Section

Vertically aligned CNT forests were grown from a patterned, iron catalyst layer on a silicon substrate by thermal chemical-vapor-deposition (CVD) methods. Briefly, the silicon substrate was patterned by photolithography and the lift-off of a catalyst stack consisting of Al_2O_3 (30 nm) and Fe (3 nm). The substrate was placed in a 1" tube furnace and the temperature was ramped to 750 °C over 10 min in hydrogen (400 sccm). When the furnace reached 750 °C, the CNTs were grown by flowing ethylene (700 sccm) and hydrogen (400 sccm). Following growth, cooling was done under argon (250 sccm). The CNTs were then put into a tube with a 16 cm diameter in a low-pressure chemical-vapor-deposition (LPCVD)[36,37] reactor. Amorphous silicon films were deposited onto the nanotubes from silane (20 sccm) at 530 °C and at 150 mtorr. To attain a uniform crystalline-silicon coating, amorphous silicon was deposited at 560 °C and then thermally annealed at 700 °C for 12–14 h.

For TLC, the SiCNTs were annealed in air at 1000 °C for 5 h to oxidize the silicon and to combust the cabon nanotubes. The SiCNT structures used for the oxidation process had continuous silicon rather than the beadlike morphology of Figure 3b. This is because the samples for oxidation started as shorter, patterned CNT structures that were coated with silicon for a longer time, resulting in thicker silicon layers and a core-shell tube morphology. The silica nanowires were then subjected to a hydrating step to increase the silanol content on the surface. The hydrating process employed a HCl: methanol (1:1) solution (0.1 M) that was heated overnight at reflux temperatures – methanol was used to aid in wetting the surface. After the hydration process, the material was rinsed thoroughly with water to remove any residual acid and was dried at 110 °C.

In addition to the CNT-M plate, a Merck TLC plate (250 μm thick sorbent layer) and a Merck HPTLC plate (150 μm thick sorbent layer) were used for comparison. The TLC plates were used to separate a CAMAG (Muttenz, Switzerland) test-dye solution that was dissolved in hexanes (3% v/v). An aliquot of the diluted test-dye mixture (0.5 μL) was spotted 5 mm from the bottom of the plate. Toluene was used as the mobile phase. A twin-trough chamber (CAMAG, Muttenz, Switzerland) was equilibrated with 3 mL of toluene for 10 min prior to chromatography. The TLC plates were developed over a 45 mm length with toluene (3 mL). The resulting developed TLC plates were digitized using a flat-bed scanner (600 × 600 dpi., MX-2300N, Sharp, Romeovill, IL).

SEM images were obtained using a Philips XL30 S-Feg instrument, operated at 5 keV. For interior views of the SiCNT structure, the wafer and SiCNT structures were broken and imaged using cross-sectional SEM. TEM and STEM observations were conducted on a FEI Tecnai F20 Analytical STEM instrument. When SiCNTs are fabricated in a forest, it is often difficult to separate the tubes for analysis. Two methods were used to prepare the TEM samples. Firstly, CNTs (before silicon coating) were scratched off the wafer into a solvent (1,2-dichloroethane). A few drops of the resulting suspension was deposited on custom-fabricated silicon TEM grids. LPCVD silicon was then deposited on the CNTs suspended across the silicon TEM grid. Although there may be a physisorbed layer on the CNTs after placement on the TEM grids (due to the suspension process), it should be removed when the CNTs are heated to 530 °C in nitrogen prior to Si deposition. This method produces a specimen without a background carbon film. Secondly, some samples were

prepared simply by scraping off the coated or oxidized structures onto a standard carbon-coated TEM grid. EELS was performed using a Gatan spectrometer (GIF – Tridiem) with the microscope run in STEM mode. Peaks in the energy-loss spectrum were used to identify elements. The fine structure was used to determine the local composition and crystal structure. Raman spectra were collected at room temperature using a PI-200 Raman analyzer equipped with a TE-cooled DU401-FI charge-coupled detector. With a grating with 1200 grooves per mm, the spectral coverage was about 2100 cm^{-1}. The data were collected using a 785.11 nm laser beam at 100 mW cm^{-2} power density.

Supporting Information

Supporting Information is available from the Wiley Online Library or from the author.

Acknowledgements

We acknowledge Professor Joel M. Harris (University of Utah) and his student ChaoXiong Ma for the acquisition of the Raman spectra. We acknowledge a BYU mentoring environment grant for student support. The TLC study was supported by US Synthetic Corporation, Orem, UT.

Author contributions: J.S. fabricated the SiCNT structures, performed the SiCNT analysis, and designed and developed the silica process for the TLC plate fabrication; D.J. performed the TLC separations and analyzed the TLC data; D.H. and B.T. performed the initial CNT growth and infiltration experiments; T.W. designed and generated the cougar pattern; M.L. conceived of the TLC application idea; R.V. and R.D. conceived of and designed the porous CNT-M process and the herringbone pattern for the TLC media. J.S. and R.D. wrote the paper.

Received: September 4, 2010
Revised: December 16, 2010
Published online: February 23, 2011

[1] B. Q. Wei, R. Vajtai, Y. Jung, J. Ward, R. Zhang, G. Ramanath, P. M. Ajayan, *Nature* **2002**, *416*, 495.
[2] S. R. Quake, A. Scherer, *Science* **2000**, *290*, 1536.
[3] J. Erlebacher, M. J. Aziz, A. Karma, N. Dimitrov, K. Sieradzki, *Nature* **2001**, *410*, 450.
[4] P. R. Bandaru, *J. Mater. Sci.* **2007**, *42*, 1809.
[5] Z. G. Wu, J. B. Neaton, J. C. Grossman, *Nano Lett.* **2009**, *9*, 2418.
[6] W. Wang, P. N. Kumta, *ACS Nano* **2010**, *4*, 2233.
[7] J. W. Coburn, H. F. Winters, *Annu. Rev. Mater. Sci.* **1983**, *13*, 91.
[8] F. Marty, L. Rousseau, B. Saadany, B. Mercier, O. Français, Y. Mita, T. Bourouina, *Microelectron. J.* **2005**, *36*, 673.
[9] S. Fan, M. G. Chapline, N. R. Franklin, T. W. Tombler, A. M. Cassell, H. J. Dai, *Science* **1999**, *283*, 512.
[10] K. Hata, D. N. Futaba, K. Mizuno, T. Namai, M. Yumura, S. Iijima, *Science* **2004**, *306*, 1362.
[11] D. N. Hutchison, N. B. Morrill, Q. Aten, B. W. Turner, B. D. Jensen, L. L. Howell, R. R. Vanfleet, R. C. Davis, *J. Microelectromech. Syst.* **2010**, *6*, 75.
[12] A. M. Morales, C. M. Lieber, *Science* **1998**, *279*, 208.
[13] M. H. Park, M. G. Kim, J. Joo, K. Kim, J. Kim, S. Ahn, Y. Cui, J. Cho, *Nano Lett.* **2009**, *9*, 3844.
[14] A. G. Cullis, L. T. Canham, *Nature* **1991**, *353*, 335.
[15] J. Sha, J. Niu, X. Ma, J. Xu, X. Zhang, Q. Yang, D. Yang, *Adv. Mater.* **2002**, *14*, 1219.
[16] X. Y. Zhang, L. D. Zhang, G. W. Meng, G. H. Li, N. Yun, J. Phillipp, F. Phillipp, *Adv. Mater.* **2001**, *13*, 1238.
[17] H. Y. Tuan, D. C. Lee, T. Hanrath, B. A. Korgel, *Nano Lett.* **2005**, *5*, 681.
[18] F. Müller, A. Birner, J. Schilling, A. P. Nielsch, K. Li, U. Gösele, V. Lehmann, *Microsyst. Technol.* **2002**, *8*, 7.
[19] B. L. Wardle, D. S. Saito, E. J. Garcia, A. J. Hart, R. G. de Villoria, E. A. Verploegen, *Adv. Mater.* **2008**, *20*, 2707.
[20] Q. Ngo, B. A. Cruden, A. M. Cassell, G. Sims, M. Meyyappan, J. Li, C. Y. Yang, *Nano Lett.* **2004**, *4*, 2403.
[21] B. C. Satishkumar, A. Govindaraj, Manashi Nath, C. N. R. Rao, *J. Mater. Chem.* **2000**, *10*, 2115.
[22] W. Q. Han, S. S. Fan, Q. Q. Li, Y. D. Hu, *Science* **1997**, *277*, 1287.
[23] W. Wang, P. N. Kumta, *J. Power Sources* **2007**, *172*, 650.
[24] J. Y. Eom, J. W. Park, H. S. Kwon, S. Rajendrana, *J. Electrochem. Soc.* **2006**, *153*, A1678.
[25] L. F. Cui, Y. Yang, C. M. Hsu, Y Cui, *Nano Lett.* **2009**, *9*, 3370.
[26] M. Liu, G. H. Lu, J. H. Chen, *Nanotechnology* **2008**, *19*, 265705.
[27] H. Bing, T Niall, R. Fred, *Anal. Chem.* **1998**, *70*, 3790.
[28] P. Gzil, N. Vervoort, G. V. Baron, G. Desmet, *Anal. Chem.* **2003**, *75*, 6244.
[29] C. Smit, R. A. C. M. M. van Swaaij, H. Donker, A. M. H. N. Petit, W. M. M. Kessels, M. C. M. van de Sanden, *J. Appl. Phys.* **2003**, *94*, 3582.
[30] J. X. Liu, J. J. Niu, D. R. Yang, M. Yan, J. Sha, *Physica E* **2004**, *23*, 221.
[31] C. Lia, G. J. Fang, S. Sheng, Z. Q. Chen, J. B. Wang, S. Ma, X. Z. Zhao, *Phys. E* **2005**, *30*, 169.
[32] S. Nakashima, M. Higashihira, K. Maeda, *J. Am. Ceram. Soc.* **2003**, *86*, 823.
[33] J. Panitz, A. Wokaun, *Appl. Spectrosc.* **1998**, *52*, 1252.
[34] P. M. Ajayan, S. Iijima, T. Ichihashi, *Phys. Rev. B: Condens. Matter* **1993**, *47*, 6859.
[35] E. Dujardin, T. W. Ebbesen, H. Hiura, K. Tanigaki, *Science* **1994**, *265*, 1850.
[36] T. I. Kamins, *J. Electrochem. Soc.: Solid-State Sci. Technol.* **1980**, *127*, 686.
[37] A. T. Voutsas, M. K. Hatalis, *J. Electrochem. Soc.* **1992**, *139*, 2659.